

## Stopping cross sections of TiO<sub>2</sub> for H and He ions

Silvina P. Limandri<sup>1</sup>, Raul C. Fadanelli<sup>2</sup>, Moni Behar<sup>2</sup>, Luiz C.C.M. Nagamine<sup>3</sup>, José M. Fernández-Varea<sup>4,a</sup>, Isabel Abril<sup>5</sup>, Rafael Garcia-Molina<sup>6</sup>, Claudia C. Montanari<sup>7</sup>, Julio C. Aguiar<sup>8</sup>, Darío Mitnik<sup>7</sup>, Jorge E. Miraglia<sup>7</sup>, and Néstor R. Arista<sup>1</sup>

<sup>1</sup> Centro Atómico Bariloche, RA-8400, San Carlos de Bariloche, Argentina

<sup>2</sup> Instituto de Física, Universidade Federal do Rio Grande do Sul, Av. Bento Gonçalves 9500, 91501-970, Porto Alegre, Brazil

<sup>3</sup> Instituto de Física, Universidade de São Paulo, 05508-090 São Paulo, São Paulo, Brazil

<sup>4</sup> Facultat de Física (ECM and ICC), Universitat de Barcelona, Diagonal 645, 08028 Barcelona, Spain

<sup>5</sup> Departament de Física Aplicada, Universitat d'Alacant, Apartat 99, 03080 Alacant, Spain

<sup>6</sup> Departamento de Física-CIOyN, Regional Campus of International Excellence "Campus Mare Nostrum", Universidad de Murcia, 30100 Murcia, Spain

<sup>7</sup> Instituto de Astronomía y Física del Espacio, CONICET and Facultad de Ciencias Exactas y Naturales, Universidad de Buenos Aires, Casilla de correo 67, Sucursal 28, C1428EGA Buenos Aires, Argentina

<sup>8</sup> Autoridad Regulatoria Nuclear, Av. Libertador 8250, C1429BNP Buenos Aires, Argentina

Received 10 December 2013 / Received in final form 16 April 2014

Published online 24 July 2014 – © EDP Sciences, Società Italiana di Fisica, Springer-Verlag 2014

**Abstract.** Stopping cross sections of TiO<sub>2</sub> films were measured for H and He ions in the energy intervals 200–1500 keV and 250–3000 keV, respectively, using the Rutherford backscattering technique. Theoretical calculations were performed by means of two versions of the dielectric formalism and a non-linear model. Good agreement is found between the present experimental data and the theoretical results at intermediate and high energies, and also with the very limited experimental information available in the literature.

### 1 Introduction

The interaction between energetic charged particles and matter has been extensively investigated since the 1940s. Penetration properties of ions in the range from a few keV/u to hundreds of MeV/u find important applications in technology [1–5] and hadron therapy [6–8], among many other fields [9], as well as in analytical techniques like Rutherford backscattering spectrometry (RBS) and nuclear reaction analysis. Surface analysis by fast ions requires knowledge on the energy loss and straggling experienced by the projectiles when they travel through the material to determine depth profiles and to estimate both mass and depth resolution [10].

There is a vast bibliography on measured stopping powers<sup>1</sup> of single-element materials for light ions [12]. On the other hand, for compounds the experimental data are very scarce and the associated uncertainties are sometimes large. The stopping cross sections (SCSs) of compounds are commonly estimated from the SCSs of the constituent elements invoking the principle of additivity of SCSs (Bragg's rule). However, this rule may lead to impor-

tant uncertainties, in particular for organic compounds, oxides and nitrides [13–15].

Theoretical calculations are helpful to supplement the existing measurements, especially when there is lack of such information. Linear (perturbative) approaches like the dielectric formalism yield accurate results if the interaction strength between the projectile and the electrons of the traversed medium can be regarded as a small perturbation; this happens when the ion charge is small and its speed much higher than that of the electrons. However, more elaborate non-linear (non-perturbative) approaches are needed to calculate realistic stopping powers at low energies, where one has to account for the strong electron-projectile coupling to all orders in the interaction.

Titanium dioxide (TiO<sub>2</sub>) is a material of growing technological interest with a broad range of applications [16–19], which can be expanded and improved by implantation with ions of intermediate and high atomic number [20]. Therefore, quantifying the rate at which ion beams deposit their energy in this substance becomes an important issue. Stopping powers for a variety of projectile-target combinations can be obtained, when direct evaluations are not available, by means of simple scaling relationships from the experimental stopping powers of light ions such as H or He [21]. In the case of TiO<sub>2</sub>, Kido and Hioki [22] published data for H projectiles albeit only at three energies, and Laube et al. [23] measured the SCS

<sup>a</sup> e-mail: jose@ecm.ub.edu

<sup>1</sup> A comprehensive overview of methods employed to measure stopping powers can be consulted in chapter 9 of reference [11].

of He ions at a single energy. In turn, Barradas et al. [24] inferred indirectly the SCS curve of He, C and O over a wide energy interval but with relatively large uncertainties around the maximum of the curve.

In the present article we report SCSs of TiO<sub>2</sub> for 200–1500 keV H ions and for 250–3000 keV He ions, measured with the RBS technique. Besides, calculations were done resorting to two versions of the dielectric formalism and a non-linear model. These theoretical frameworks offer complementary pictures of the energy loss processes undergone by ions moving in solids. The present and earlier measurements are compared to the corresponding calculations and to the semi-empirical predictions of the SRIM code [25].

## 2 Experimental methods and data analysis

### 2.1 Sample preparation and characterization

The radio-frequency magnetron sputtering technique, with a commercial TiO<sub>2</sub> (rutile) target and an O<sub>2</sub>/Ar mixture as sputtering gas, was used to deposit TiO<sub>2</sub> films on thick C or Si substrates. A Rigaku  $\theta$ – $2\theta$  diffractometer (Cu K $\alpha$  X-rays) was utilized to carry out low- and high-angle diffraction scans of the samples with Si substrate. The thickness, root-mean-square roughness and mass density of the TiO<sub>2</sub> films were deduced from the best fit of simulations done with Philips' WinGIXA software [26,27] to the experimental X-ray reflectivity data. The thicknesses of the TiO<sub>2</sub> films were 146(3), 114(3), 79(1), 60(1) and 30(1) nm, and the respective roughnesses were estimated to be 1.5(2), 1.2(2), 0.6(1), 0.6(1) and 0.6(1) nm. The average mass density of TiO<sub>2</sub> was 3.8(2) g/cm<sup>3</sup>, where the uncertainty was calculated by the standard deviation of the density values obtained from the fits. This value of the mass density is similar to that found by Laube et al. [23] and Drogowska et al. [28] in films whose thicknesses are comparable to ours. Figure 1 displays some of the measured and fitted X-ray reflectivity spectra; an excellent accord between the simulated reflectivity curves and the experimental values can be seen, especially for the 79 nm and 114 nm films. The mass density of TiO<sub>2</sub> in the samples with C substrate was assumed to be also 3.8(2) g/cm<sup>3</sup>, and the thicknesses of the films were estimated by comparing the widths of the Ti structure in the RBS spectra corresponding to TiO<sub>2</sub> deposited on C and on Si. The resulting thicknesses were 260(4), 170(3), 78(2) and 40(1) nm. The stoichiometry of the films was checked by means of RBS and found to be compatible with TiO<sub>2</sub> within 10%.

### 2.2 RBS measurements

The measurements were conducted at the Instituto de Física da Universidade Federal do Rio Grande do Sul, Brazil, with <sup>1</sup>H<sup>+</sup> and <sup>4</sup>He<sup>+</sup> ion beams delivered by the 500 kV ion implanter for the lower energies and the 3 MV Tandem accelerator for the higher ones. The sample

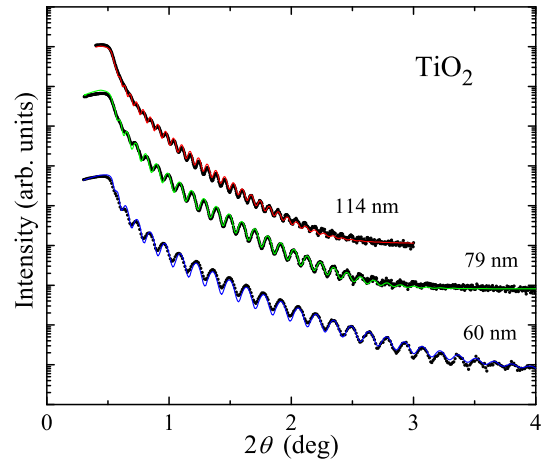


**Fig. 1.** Measured X-ray reflectivity spectra (symbols) and corresponding WinGIXA simulated spectra (solid curves) for three Si(100)/TiO<sub>2</sub> samples, labelled with the thicknesses of the corresponding TiO<sub>2</sub> films.

chosen for each energy was selected to keep the Ti structure in the RBS spectra as well defined as possible. For the measurements with H<sup>+</sup> beams we used the films deposited on C substrates in order to avoid the overlap of the Si and Ti structures in the spectra. In some cases, two samples were irradiated at the same energy, yielding quite compatible results.

The RBS measurements were carried out in the so-called IBM geometry [29], fixing the detector position at the scattering angle  $\theta = 120^\circ$  with respect to the beam direction. For each beam energy four spectra were recorded at incidence angles  $\theta_0 = 0^\circ, 20^\circ, 40^\circ$  and  $60^\circ$  between the sample normal and the beam direction. The corresponding angles between the sample normal and the detector direction are given by  $\theta_1 = 180^\circ - \theta - \theta_0$ . The RBS spectra were acquired with a Si surface barrier detector coupled to standard electronics and a multichannel analyzer. The total detector plus electronics resolution (FWHM) was around 8 keV for H and 11 keV for He. Typical spectra pertaining to 1500 keV <sup>1</sup>H<sup>+</sup> and 800 keV <sup>4</sup>He<sup>+</sup> beams are shown in Figures 2 and 3, respectively.

### 2.3 Data analysis

The fundamental expression in the backscattering method is [29]

$$\frac{K}{\cos \theta_0} S_{\text{in}} + \frac{1}{\cos \theta_1} S_{\text{out}} = \frac{E_{1,\text{max}} - E_{1,\text{min}}}{d}, \quad (1)$$

where  $K$  is the kinematic factor and  $d$  is the film thickness.  $E_{1,\text{max}}$  and  $E_{1,\text{min}}$  are, respectively, the front and back energy edges of the Ti structure observed in the RBS spectrum (see Figs. 2 and 3); they are obtained by fitting the Ti structure to an analytical expression (the sum of an error function and a complementary error function, multiplied by a power of energy to allow for the energy dependence of the elastic differential cross section). The unknowns in

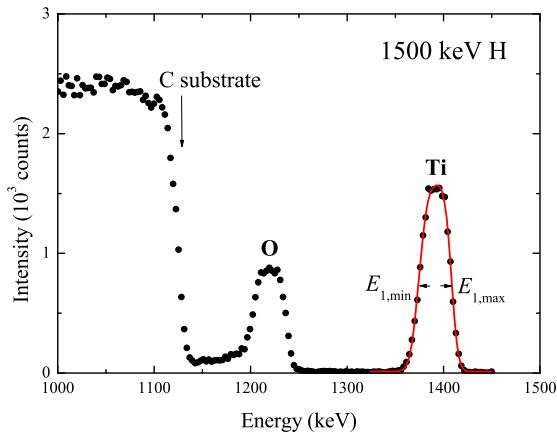


**Fig. 2.** RBS spectrum (dots) resulting from the 260-nm-thick  $\text{TiO}_2$  film on C bombarded by a 1500 keV  $^1\text{H}^+$  beam (normal incidence). The curve is the fit of the Ti structure. The horizontal arrows indicate the  $E_{1,\min}$  and  $E_{1,\max}$  energies.

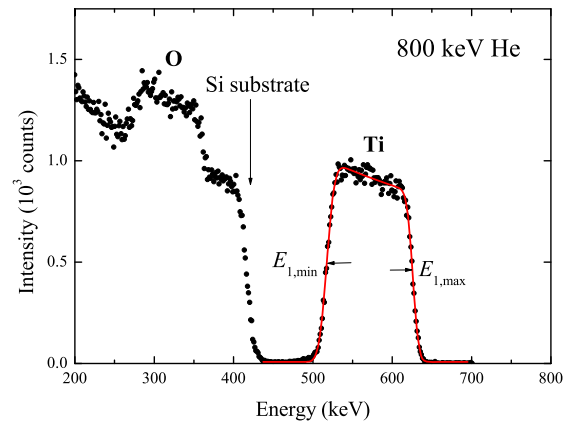


**Fig. 3.** RBS spectrum (dots) resulting from the 79-nm-thick  $\text{TiO}_2$  film on Si bombarded by a 800 keV  $^4\text{He}^+$  beam (normal incidence). The curve is the fit of the Ti structure. The horizontal arrows indicate the  $E_{1,\min}$  and  $E_{1,\max}$  energies.

equation (1) are the stopping powers  $S_{\text{in}} \equiv S(\bar{E}_{\text{in}})$  and  $S_{\text{out}} \equiv S(\bar{E}_{\text{out}})$  at the also unknown energies  $\bar{E}_{\text{in}}$  and  $\bar{E}_{\text{out}}$ , which are the average kinetic energies of the ions along the incoming and outgoing paths in the film. A system of equations must be established to solve for  $S_{\text{in}}$  and  $S_{\text{out}}$ . This was done by measuring, for each incident energy  $E_0$ , the RBS spectra at four geometries (i.e., combinations of  $\theta_0$  and  $\theta_1$ ) as mentioned above. Then,  $S_{\text{in}}$  and  $S_{\text{out}}$  were taken as the mean values of the six possible solutions of the overdetermined system of equations [30], and were transformed into SCSs using the average mass density of the films. Finally,  $\bar{E}_{\text{in}}$  and  $\bar{E}_{\text{out}}$  are evaluated from the mean-energy approximation [29].

The uncertainty budget includes the standard deviation of the mean values of the SCSs and the uncertainties related to the film thickness and mass density, yielding uncertainties around 11% and 7% (1 SD) for H and He, respectively. The data for H are affected by larger uncertainties due to the narrow Ti structures in the RBS spectra, which are difficult to fit, especially at low energies.

### 3 Theoretical stopping powers

Several theoretical approaches exist to describe the energy loss of ions in matter, each having advantages and drawbacks [3]. Consider a heavy charged particle, with atomic number  $Z_1$ , that moves at non-relativistic speed  $v$  (kinetic energy  $E$ ) through a medium. In the energy interval of present concern, excitations and ionizations of the target electrons are the main energy-loss mechanisms, which are quantified by the electronic stopping power. Electron capture and loss events take also place, changing dynamically the number of electrons  $N_b$  bound to the projectile. After a few collisions, an equilibrium charge state  $q = Z_1 - N_b$  is reached which depends on  $Z_1$ ,  $v$  and the electronic excitation spectrum of the traversed medium. The stopping power  $S(v)$  is then equal to the sum of the partial stopping powers  $S_q(v)$  pertaining to each charge state  $q$  weighted

with the associated charge-state fraction  $\phi_q(v)$ ; that is:

$$S(v) = \sum_{q=0}^{Z_1} \phi_q(v) S_q(v). \quad (2)$$

The theoretical stopping powers (energy loss per unit path length) are converted to SCSs (energy times area, per atom) dividing by the atomic density of the medium.

To our knowledge, no experimental data for the equilibrium charge-state fractions of H or He through bulk  $\text{TiO}_2$  have been reported. Thus, following reference [31] we assume that  $\phi_q(v)$  has a Gaussian shape with parameters determined from the mean equilibrium charge-state formula fitted by Schiwietz and Grande to experimental data [32].

We summarize below the three methodologies chosen to calculate  $S_q(v)$ . On one hand, the MELF-GOS (Mermin Energy-Loss Function – Generalized Oscillator Strength) and SLPA (Shellwise Local Plasma Approximation) approaches are based on the dielectric formalism, sharing the limitations inherent to a first-order perturbative theory but with accurate results at intermediate and high velocities. On the other hand, the non-perturbative TCS-EFSR (Transport Cross Section – Extended Friedel Sum Rule) model includes all orders in the electron-ion interaction strength and incorporates dynamic screening effects, being therefore particularly adequate to describe the stopping of projectiles with arbitrary velocities in a homogeneous electron gas.

#### 3.1 Linear-response approximations

In the dielectric formalism the stopping power of a material for a swift projectile is written as [33,34]

$$S_q(v) = \frac{2e^2}{\pi v^2} \int_0^\infty \frac{dk}{k} [Z_1 - \rho_q(k)]^2 \int_0^{kv} d\omega \omega \text{Im} \left[ \frac{-1}{\epsilon(k, \omega)} \right]. \quad (3)$$

An advantage of this formalism is the decoupling of the projectile and target properties. The projectile is characterized by its velocity  $v$  and the Fourier transform of its electronic charge distribution,  $\rho_q(k)$  [31,35]. The nature of the stopping substance enters solely through its electronic excitation spectrum, encoded in its energy-loss function (ELF)  $\text{Im}[-1/\epsilon(k, \omega)]$ , where  $\epsilon(k, \omega)$  is the dielectric function that accounts for electronic excitations with momentum and energy transfers  $\hbar k$  and  $\hbar\omega$ , respectively.

We employ two fully independent versions of the dielectric formalism, namely the MELF-GOS and SLPA approaches. The former describes realistically the whole excitation spectrum of the considered material from a fit to its optical ELF (i.e., at  $k = 0$ ). The latter models separately the contributions of the deeply-bound, valence and conduction-band electrons to the ELF if reliable theoretical wave functions and binding energies are available as input data.

### 3.1.1 The MELF-GOS method

In the MELF-GOS method [31,36,37], the excitation spectrum of the valence electrons is accounted for through a fit of Mermin-type ELF's [38] to the available optical ELF of the studied substance, whereas the contribution of the inner-shell electrons to the excitation spectrum is derived from their GOSs at  $k = 0$  because they retain an atomic character. Besides reproducing reasonably the main features that appear in the optical ELF, physically motivated restrictions such as the  $f$ -sum rule must be fulfilled by the resulting ELF. The MELF-GOS method readily furnishes an analytical extension of the fitted optical ELF to finite momentum transfers ( $k \neq 0$ ). In this manner, the electronic stopping power, equation (3), can be easily computed numerically for every charge state  $q$ . Furthermore, we have added to equation (3) the correction term that originates in the polarization of a dressed projectile [39] and, for H ions, an extra term that incorporates the stopping power caused by electron capture and loss processes [39].

In the case of  $\text{TiO}_2$ , the K shells of Ti and O and the L subshells of Ti are described with non-relativistic hydrogenic GOSs (see e.g. Ref. [31]). The optical ELF corresponding to the weakly-bound electrons is fitted to the data calculated with density functional theory (DFT) by Dash et al. [40]. Although Fuentes et al. [41] measured and parameterized the optical ELF of  $\text{TiO}_2$ , their parameterization is not suitable for the present purposes because it yields, through the finite-energy  $f$ -sum rule a too small number of valence electrons. Landmann et al. [42] calculated with DFT the optical ELF but only up to 14 eV, which is insufficient for our intent. Figure 4 displays the ELF of  $\text{TiO}_2$  in the optical limit as a function of energy transfer. The ab initio calculations by Dash et al. [40] and the fitted sum of Mermin ELF's are plotted together with the DFT values of Landmann et al. [42] and the existing experimental data [43].

The mean excitation energy  $I$ , which is the only non trivial material property in Bethe's asymptotic stopping

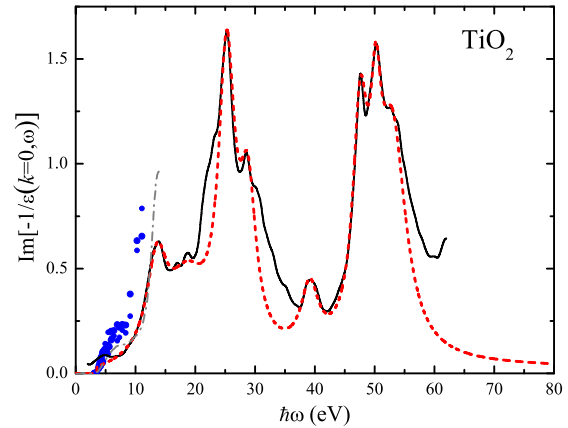


**Fig. 4.** Optical ELF of  $\text{TiO}_2$  as a function of  $\hbar\omega$ . The continuous curve represents the ab initio values computed by Dash et al. [40]. The dashed curve corresponds to the optical ELF fitted with the MELF-GOS method [31,36,37]. The optical ELF calculated by Landmann et al. [42] is represented as a dot-dashed curve. The symbols are experimental data taken from reference [43].

power formula [11], can be also deduced from the optical ELF [11]. For  $\text{TiO}_2$ , the MELF-GOS method gives  $I = 164$  eV, about 10% smaller than the value  $I = 179.5$  eV recommended in reference [44].

### 3.1.2 The SLPA

Within the SLPA the dielectric response is evaluated separately for each electron sub-shell of the medium (atom or compound), describing them as an electron cloud with a binding energy. To this end, the Levine-Louie dielectric function [45] is adopted. The SLPA has been already employed to calculate total and differential ionization cross sections, stopping powers and other moments of the energy-loss distribution [35,46,47]. In practice, it has been applied to different materials including metals, insulators and gases; here we describe the first attempt to model electronic excitations in a semiconductor.

We obtained the wave functions and binding energies of electrons in  $\text{TiO}_2$  resorting to DFT with the generalized-gradient approximation (GGA). The calculations were carried out for the  $\text{Ti}^{4+}\text{O}_2^{2-}$  configuration, i.e. with the valence band fully occupied (6 electrons in the O 2p orbital, binding energy equal to 6.7 eV). The radial wave functions of core electrons, the pseudo-potentials and the pseudo-atomic orbitals of valence electrons were generated by means of the `OpenMX` and `ADPACK` codes<sup>2</sup>, which implement the non-relativistic Kohn-Sham equations under the GGA with a Troullier and Martins scheme [48]. Electronic orbitals of Ti metal have been reported previously [49] using the same model.

We assumed  $\text{TiO}_2$  to be in the rutile phase (tetragonal crystal system, space group  $P4_2/mnm$ ). Energy minimization yields a cohesive energy per molecule

<sup>2</sup> <http://www.openmx-square.org/>

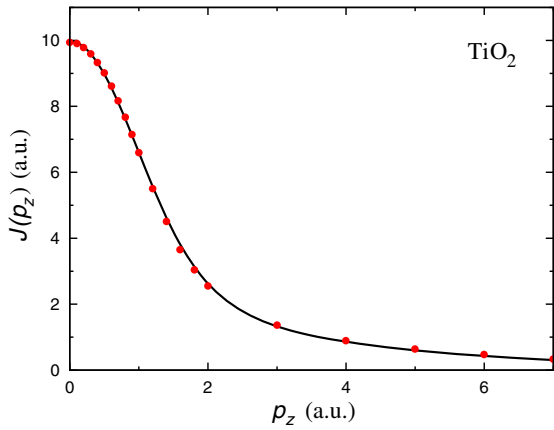


**Fig. 5.** Compton profile of  $\text{TiO}_2$ . The solid curve indicates the present DFT-GGA calculation, whereas the circles are the experimental data from reference [51].

of  $-18.29$  eV, which is attained for lattice constants  $a = 4.59$  Å and  $c = 2.96$  Å. These values are close to the experimental cohesive energy of  $-19.9$  eV and the measured lattice constants  $a = 4.5937$  Å and  $c = 2.9618$  Å [50].

The applicability of the DFT-GGA framework to a complex system such as  $\text{TiO}_2$  was checked by testing the Compton profile that results from our wave functions with available experimental data. The Compton profile is a powerful tool to extract information on the electronic structure of a system owing to the strong relationship between the motion of the target electrons and Doppler line-broadening of the spectrum collected in the inelastic scattering of  $x$ - and  $\gamma$ -rays with electrons (see [49] and references therein). Within the impulse approximation, the Compton profile of the  $n\ell$  orbital is defined as:

$$J_{n\ell}(p_z) = 2\pi \int_{|p_z|}^{\infty} \rho_{n\ell}(p) p dp, \quad (4)$$

where  $p_z$  is the projection of the momentum transfer on the electron linear momentum before the collision and the spherically-symmetrical electron density in momentum space,  $\rho_{n\ell}(p)$ , is related to the Fourier transform of the  $n\ell$  radial wave function. The Compton profile of a  $\text{TiO}_2$  molecule is  $J(p_z) = \sum_{n\ell} Z_{n\ell} J_{n\ell}(p_z)$ , being  $Z_{n\ell}$  the number of electrons in the  $n\ell$  orbital. In Figure 5, the theoretical  $J(p_z)$  is compared to the measurement done by Gupta [51] on polycrystalline rutile. There is good agreement between the prediction of DFT-GGA and the experimental values. Joshi and Sharma [52] had found a similar accord between their ab initio periodic Hartree-Fock calculations with linear combination of atomic orbitals and Gupta's experiment.

The DFT-GGA provides the wave functions of the ground state, with all the electrons in the valence band. A controversial point when describing the energy loss in semiconductors is how many electrons remain in the valence band and how many of them are in the conduction band (the band gap is 3 eV [53]). The theoretical prediction and the interpretation of the experimental spectra has been widely discussed in references [40,54].

We implement the SLPA as in previous works [46], combining bound electrons and a free-electron gas, keeping the total number of electrons unchanged. In the case of  $\text{TiO}_2$ , bound electrons were described through the DFT-GGA wave functions and binding energies, with a vacancy in the valence band of one of the two O atoms and one electron per molecule in the conduction band. The latter constitute a free-electron gas with  $r_s = 3.69$  and damping constant  $\gamma = 5$  eV. This choice is consistent with the band gap of 3 eV [53] between the valence band (recall the aforementioned binding energy of the O 2p orbital, 6.7 eV) and a single electron in the conduction band (Fermi energy of 3.7 eV).

### 3.2 The TCS-EFSR model

Lifschitz and Arista [55] developed a non-linear formalism, hereafter referred to as TCS-EFSR, that is able to describe the energy loss of ions with arbitrary velocities in a homogeneous degenerate electron gas. The electronic stopping power is evaluated from the energy transfer associated to the elastic electron-ion collisions in the reference frame of the moving ion (kinetic theory [56]) averaged over the distribution of electron velocities [55,57],

$$S_q(v) = \frac{1}{16\pi^2} \frac{m_e^4}{\hbar^3} \frac{1}{v^2} \int_{|v-v_F|}^{v+v_F} dv_r v_r^2 \sigma_{\text{tr}}(v_r; v) \times [v_r^2 - (v - v_F)^2] [(v + v_F)^2 - v_r^2], \quad (5)$$

where  $v_F$  is the Fermi velocity of the electron gas and  $v_r$  is the relative velocity in the binary collision. In turn, the TCS is given by the expansion

$$\sigma_{\text{tr}}(v_r; v) = \frac{4\pi}{(m_e v_r / \hbar)^2} \sum_{\ell=0}^{\infty} (\ell + 1) \times \sin^2[\delta_{\ell}(v_r; v) - \delta_{\ell+1}(v_r; v)], \quad (6)$$

with the phase shifts  $\delta_{\ell}$  computed numerically by solving the radial Schrödinger equation for the electron-ion interaction potential, which may have two contributions. When  $N_b \neq 0$  ( $\text{H}^0$ ,  $\text{He}^+$ ,  $\text{He}^0$ ), the potential due to the projectile electron(s) is hydrogenic. A Yukawa potential,  $-(qe^2/r) e^{-\alpha r}$ , is added to account for screening effects by the electron gas if  $q \neq 0$  ( $\text{H}^+$ ,  $\text{He}^+$ ,  $\text{He}^{2+}$ ). The screening parameter  $\alpha$  is adjusted self-consistently imposing that the phase shifts fulfil the EFSR [55]

$$Z_1 = \frac{2}{\pi} \sum_{\ell=0}^{\infty} (2\ell + 1) \int_{|v-v_F|}^{v+v_F} dv_r \frac{v_r^2 + v_F^2 - v^2}{4v_r^2 v} \delta_{\ell}(v_r; v) + N_b \Theta(v - v_F). \quad (7)$$

Notice that the phase shifts and the ensuing TCS depend implicitly on the speed of the ion because, through the EFSR, the screening parameter and hence the interaction potential are functions of  $v$ .

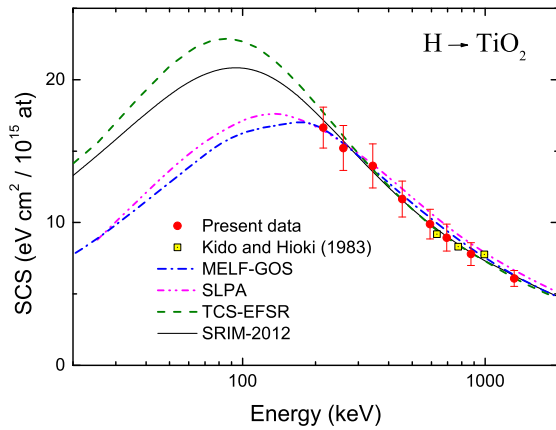


**Fig. 6.** SCSs of  $\text{TiO}_2$  for H ions as a function of the projectile kinetic energy. The circles are the present experimental data. The squares correspond to the measurements done by Kido and Hioki [22] (uncertainties smaller than the symbol size). The dot-dashed, double-dot-dashed and dashed curves are the SCSs calculated with the MELF-GOS, SLPA and TCS-EFSR models, respectively, whereas the solid curve indicates semi-empirical values from SRIM [25].

In the present calculations with the TCS-EFSR model we have assumed that the valence electrons of  $\text{TiO}_2$  constitute a homogeneous electron gas characterized by an effective one-electron radius  $r_s = 1.35$  (plasmon energy of 30 eV). The TCS-EFSR SCSs for the various charge states of the projectiles were weighted with the respective velocity-dependent charge fractions and added, see equation (2).

## 4 Results and discussion

The SCSs of  $\text{TiO}_2$  for H and He ions are shown in Figures 6 and 7, respectively, as a function of the projectile's kinetic energy. The present experimental values are depicted along with the predictions of the three theoretical approaches outlined above. The SRIM SCSs, calculated with the Bragg rule from the elemental stopping powers of Ti and O, are also plotted in the figures for comparison purposes.

It can be seen in Figures 6 and 7 that the SCSs from SRIM match closely the experimental data of H and He, even around the maximum of the SCS of He. This seems to indicate that the Bragg rule is applicable to  $\text{TiO}_2$ .

Kido and Hioki [22] measured stopping powers of H ions in  $\text{TiO}_2$  by means of nuclear reaction analysis. The ensuing SCSs, displayed in Figure 6, have uncertainties around 6%. These results are in excellent agreement with our measurements, although they cover a rather limited energy interval.

Laube and associates [23] measured the SCS of 2300 keV He projectiles in four  $\text{TiO}_2$  samples having recourse to the RBS method. Our results are consistent with their values, included in Figure 7. The experimental data of Barradas et al. [24] for He ions are also shown in Figure 7. These authors acquired RBS spectra at a few energies and backscattering angles, fitting them

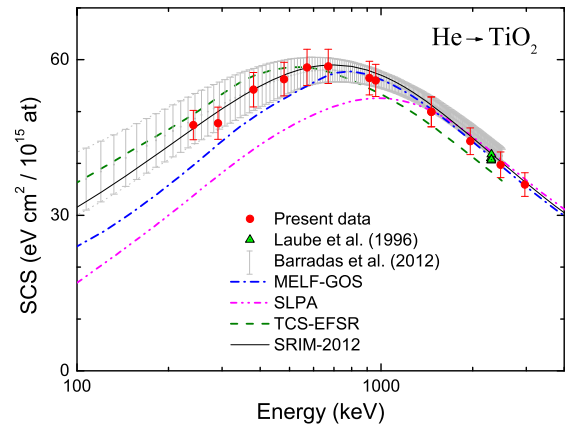


**Fig. 7.** SCSs of  $\text{TiO}_2$  for He ions as a function of the projectile kinetic energy. The circles are the present experimental data. The triangles correspond to the measurements done by Laube et al. [23] and the curve delimited by vertical bars is the result of Barradas et al. [24]. The dot-dashed, double-dot-dashed and dashed curves are the SCSs calculated with the MELF-GOS, SLPA and TCS-EFSR models, respectively, whereas the solid curve indicates semi-empirical values from SRIM [25].

simultaneously with a Bayesian inference Markov chain Monte Carlo algorithm. This indirect data-analysis procedure resulted in an SCS curve with a wide confidence band (larger than 20% for energies below 400 keV). Anyhow, the fair agreement between the present SCSs, which span a broad energy interval, and those of Barradas et al. lends support to their analysis method.

The three theoretical calculations are in satisfactory accord with the experimental values for H in  $\text{TiO}_2$  at kinetic energies larger than around 200 keV. On the other hand, in the case of He the MELF-GOS curve matches the experimental data above 800 keV, whereas the SLPA SCSs only merges with the measurements above 1500 keV. Nevertheless, the SLPA values at high energies support the reliability of the DFT-GGA wave functions for the  $\text{TiO}_2$  molecule, which were evaluated specifically for the present work. In the opposite regime of intermediate and low energies the MELF-GOS and SLPA models progressively lose validity, as expected for perturbative approximations. The situation is further complicated at these energies by the co-existence of various projectile charge states. For its part, the non-linear TCS-EFSR model performs better than the perturbative approaches around and below the maximum of the SCS, although it seems to predict slightly too large values. Interestingly, the TCS-EFSR SCSs for He underestimate the experimental results at high energies, perhaps because all valence electrons are regarded as forming a homogeneous free-electron gas.

## 5 Conclusions

SCSs of  $\text{TiO}_2$  for H and He ions were measured at energies from 200 to 1500 keV and from 250 to 3000 keV, respectively. The experimental data presented in this work are, to our knowledge, the first ones in such extended energy intervals.

The SRIM semi-empirical SCSs agree very well with the present measurements, even around the maximum of the SCS for He ions. In addition, the theoretical predictions of the MELF-GOS, SLPA and TCS-EFSR approaches have been compared to the experimental data. The three calculations successfully reproduce the measurements above some 300 keV/u, but the differences between the theoretical SCSs are appreciable at lower energies.

Three main factors influence the present theoretical results and remain open to future developments. The first one is the description of the conduction band of TiO<sub>2</sub>, i.e. the wave functions and also the ELF for energy transfers below 10 eV. The second one is the equilibrium charge fractions of H and He in TiO<sub>2</sub>. Our theoretical SCSs for the various projectile charge states are weighted with semi-empirical charge fractions and are very sensitive to these values. The absence of experimental charge states pertaining to H and He in TiO<sub>2</sub> casts doubts on the SCS at low and intermediate energies. In fact, the existence of neutral H is open to question, at least in metals. On the contrary, for energies above the SCS maximum where one expects to have mostly bare ions, all the theoretical SCSs agree reasonably well with the measurements. The third factor is the importance of a non-linear description, at least for He (and heavier ions), that takes into account an accurate representation of the conduction band of TiO<sub>2</sub>.

We thank the financial support from the Spanish Ministerio de Economía y Competitividad (Projects FPA2009-14091-C02-01 and FIS2010-17225) and the European Regional Development Fund. This work was partially supported by the following Argentinian institutions: Consejo Nacional de Investigaciones Científicas y Técnicas (CONICET), Agencia Nacional de Promoción Científica y Tecnológica (ANPCyT). N. Vast and N.P. Barradas kindly provided us with their data. We are indebted to F. Yubero and M. Landmann for clarifying discussions.

## References

1. *Materials Modification by High-fluence Ion Beams*, NATO-ASI Series E: Applied Sciences, edited by R. Kelly, M.F. da Silva (Kluwer Academic Publishers, Dordrecht, 1989), Vol. 155
2. S.A. Campbell, *The Science and Engineering of Microelectronic Fabrication* (Oxford University Press, Oxford, 1996)
3. M. Nastasi, J.W. Mayer, J.K. Hirvonen, *Ion-Solid Interactions: Fundamentals and Applications* (Cambridge University Press, Cambridge, 1996)
4. J.K.N. Lindner, A.N. Larsen, J.M. Poate, E.E.B. Campbell, R. Kelly, G. Marletta, M. Toulemonde, F. Priolo, *New Trends in Ion Beam Processing of Materials and Beam Induced Nanometric Phenomena (European Materials Research Society Symposia Proceedings)* (Elsevier, 1997), Vol. 65
5. *Materials Science with Ion Beams*, edited by H. Bernas (Springer, Berlin, 2010)
6. D. Schardt, T. Elsässer, D. Schulz-Ertner, *Rev. Mod. Phys.* **82**, 383 (2010)
7. *Proton Therapy Physics*, edited by H. Paganetti (CRC Press, Boca Raton, 2012)
8. *Theory of Heavy Ion Collision Physics in Hadron Therapy*, Advances in Quantum Chemistry, edited by Dz. Belkic (Elsevier, Amsterdam, 2013), Vol. 65
9. *Application of Accelerators in Research and Industry: Twenty-Second International Conference*, edited by F.D. McDaniel, B.L. Doyle, G.A. Glass, Y. Wang, in AIP Conf. Proc., Vol. 1525 (2013)
10. E. Rauhala, N.P. Barradas, S. Fazinic, M. Mayer, E. Szilágyi, M. Thompson, *Nucl. Instrum. Methods Phys. Res. B* **244**, 436 (2006)
11. International Commission on Radiation Units and Measurements, *Stopping Powers and Ranges for Protons and Alpha Particles*, ICRU Report 49 (ICRU, Bethesda, MD, 1993)
12. H. Paul, Stopping Power for Light Ions, <http://www.exphys.jku.at/stopping/>
13. W. Neuwirth, W. Pietsch, K. Richter, U. Hauser, *Z. Phys. A* **275**, 215 (1975)
14. R.B. Brown, D. Powers, *J. Appl. Phys.* **50**, 5099 (1979)
15. P. Bauer, D. Semrad, *Adv. Quantum Chem.* **46**, 153 (2004)
16. U. Diebold, *Surf. Sci. Rep.* **48**, 53 (2003)
17. M. Ni, M.K.H. Leung, D.Y.C. Leung, K. Sumathy, *Renew. Sustain. Energy Rev.* **11**, 401 (2007)
18. X. Chen, S.S. Mao, *Chem. Rev.* **107**, 2891 (2007)
19. D. Kowalski, D. Kim, P. Schmuki, *Nano Today* **8**, 235 (2013)
20. A.L. Stepanov, *Rev. Adv. Mater. Sci.* **30**, 150 (2012)
21. C.P. Race, D.R. Mason, M.W. Finnis, W.M.C. Foulkes, A.P. Horsfield, A.P. Sutton, *Rep. Prog. Phys.* **73**, 116501 (2010)
22. H. Kido, T. Hioki, *Phys. Rev. B* **27**, 2667 (1983)
23. M. Laube, F. Rauch, C. Ottermann, O. Anderson, K. Bange, *Nucl. Instrum. Methods Phys. Res. B* **113**, 288 (1996)
24. N.P. Barradas, E. Alves, Z. Siketic, I. Bogdanovic Radovic, *Nucl. Instrum. Methods Phys. Res. B* **273**, 22 (2012)
25. J.F. Ziegler, J. Biersack, *SRIM-2012, The Stopping and Range of Ions in Matter*, version 2012, code available from <http://www.srim.org>
26. A.J.G. Leenaers, D.K.G. de Boer, *X-Ray Spectrom.* **26**, 115 (1997)
27. L.C.C.M. Nagamine, A. Biondo, L.G. Pereira, A. Mello, J.E. Schmidt, T.W. Chimendes, J.B.M. Cunha, E.B. Saitovitch, *J. Appl. Phys.* **94**, 5881 (2003)
28. K. Drogowska, Z. Tarnawski, A. Brudnik, E. Kusior, M. Sokolowski, K. Zakrzewska, A. Reszka, N.-T.H. Kim-Ngan, A.G. Balogh, *Mater. Res. Bull.* **47**, 296 (2012)
29. W.K. Chu, J.W. Mayer, M.A. Nicolet, *Backscattering Spectrometry* (Academic Press, New York, 1978)
30. G.H. Lantschner, J.C. Eckardt, A.F. Lifschitz, N.R. Arista, L.L. Araujo, P.F. Duarte, J.H.R. dos Santos, M. Behar, J.F. Dias, P.L. Grande, C.C. Montanari, J.E. Miraglia, *Phys. Rev. A* **69**, 062903 (2004)
31. S. Heredia-Avalos, R. Garcia-Molina, J.M. Fernández-Varea, I. Abril, *Phys. Rev. A* **72**, 052902 (2005)
32. G. Schiwietz, P.L. Grande, *Nucl. Instrum. Methods Phys. Res. B* **175**, 125 (2001)
33. J. Lindhard, K. Dan. Vidensk. Selsk. Mat. Fys. Medd. **288(8)**, (1954)
34. D. Emfietzoglou, in *Interaction of Radiation with Matter* edited by H. Nikjoo, S. Uehara, D. Emfietzoglou (CRC Press, Boca Raton, 2012), Section III
35. C.C. Montanari, D.M. Mitnik, J.E. Miraglia, *Radiat. Eff. Defects Solids* **166**, 338 (2011)

36. P. de Vera, I. Abril, R. Garcia-Molina, J. Appl. Phys. **109**, 094901 (2010)
37. R. Garcia-Molina, I. Abril, I. Kyriakou, D. Emfietzoglou, in *Radiation Damage in Biomolecular Systems, Biological and Medical Physics, Biomedical Engineering*, edited by G.G. Gómez-Tejedor, M.C. Fuss (Springer, Dordrecht, 2012), Chap. 15
38. N.D. Mermin, Phys. Rev. B **1**, 2362 (1970)
39. C.D. Denton, I. Abril, J.C. Moreno-Marín, S. Heredia-Avalos, R. Garcia-Molina, Phys. Stat. Sol. B **245**, 1498 (2008)
40. L.K. Dash, F. Bruneval, V. Trinité, N. Vast, L. Reining, Comput. Mater. Sci. **38**, 482 (2007)
41. G.G. Fuentes, E. Elizalde, F. Yubero, J.M. Sanz, Surf. Interf. Anal. **33**, 230 (2002)
42. M. Landmann, T. Köhler, S. Köppen, E. Rauls, T. Frauenheim, W.G. Schmidt, Phys. Rev. B **86**, 064201 (2012)
43. *The Electronic Handbook of Optical Constants of Solids* edited by E.D. Palik, G. Ghosh (Academic Press, San Diego, 1999)
44. International Commission on Radiation Units and Measurements, *Stopping Powers for Electrons and Positrons*, ICRU Report 37 (ICRU, Bethesda, MD, 1984)
45. Z.H. Levine, S.G. Louie, Phys. Rev. B **25**, 6310 (1982)
46. E.D. Cantero, R.C. Fadanelli, C.C. Montanari, M. Behar, J.C. Eckardt, G.H. Lantschner, J.E. Miraglia, N.R. Arista, Phys. Rev. A **79**, 042904 (2009)
47. C.C. Montanari, J.E. Miraglia, in *Theory of Heavy Ion Collision Physics in Hadron Therapy*, Advances in Quantum Chemistry, edited by Dz. Belkic (Elsevier, Amsterdam, 2013), Vol. 65, Chap. 7
48. N. Troullier, J.L. Martins, Phys. Rev. B **43**, 1993 (1991)
49. J.C. Aguiar, H.O. Di Rocco, D. Mitnik, J. Phys. Chem. Solids **74**, 1341 (2013)
50. *CRC Handbook of Chemistry and Physics*, edited by D.R. Lide, 89th edn. (CRC Press, Boca Raton, 2009)
51. A. Gupta, Ph.D. thesis, University of Rajasthan, Jaipur, 1987
52. K.B. Joshi, B.K. Sharma, J. Alloys Compd. **440**, 51 (2007)
53. C.E. Ekuma, D. Bagayoko, Jpn J. Appl. Phys. **50**, 101103 (2011)
54. N. Vast, L. Reining, V. Olevano, P. Schattschneider, B. Jouffrey, Phys. Rev. Lett. **88**, 037601 (2002)
55. A.F. Lifschitz, N.R. Arista, Phys. Rev. A **57**, 200 (1998)
56. L. de Ferrariis, N.R. Arista, Phys. Rev. A **29**, 2145 (1984)
57. H.B. Nersisyan, A.K. Das, Nucl. Instrum. Methods Phys. Res. B **227**, 455 (2005)